Cooperative stator assembly of bacterial flagellar motor for autonomous torque regulation

Kenta I. Ito[a], Shuichi Nakamura[a], and Shoichi Toyabe[a, *]

[a]Department of Applied Physics, Graduate School of Engineering, Tohoku University, Aoba 6-6-05, Sendai 980-8579, Japan
[*]toyabe@tohoku.ac.jp

ABSTRACT

Cooperativity has a central place in biological regulation, providing robust and highly-sensitive regulation. The bacterial flagellar motor (BFM) implements autonomous torque regulation by the nonequilibrium structure of the stators; the stators assemble at high load and disperse at low load. It would be natural to suppose that the stator packing is affected by stator-stator interaction. However, the cooperativity among the stators has rarely been explored. Here, we evaluated the energetics and kinetics of the stator assembly by combining dynamic load control of a single motor and the trajectory analysis based on statistical mechanics. We demonstrate that the BFM exploits the dynamic cooperativity of the stator binding for the autonomous torque regulation. The cooperative assembly leads to a discontinuous phase transition and hysteresis, which may implement torque regulation with high sensitivity and robustness.

Motility regulation is vital and the basis of autonomy for many life forms. Swimming bacteria like *Escherichia coli* and *Salmonella enterica* have been serving as the model system of the motility regulation. Since they utilize the propulsive force of the rotating flagella, the motility regulation is basically equivalent to the torque regulation of the flagellar motor. The bacterial flagellar motor (BFM)[1–5] (Fig. 1A) is a large protein complex and can rotate at up to 1,700 Hz[6], reverse the rotation, and vary the torque depending on the load on the motor. A striking fact is that the BFM has multiple torque-generating stators and regulates the torque magnitude by dynamically alternating the stators between the motor and surrounding membrane pool[7–22] (Fig. 1B). This autonomous stator assembly relies on the self-regulation of each stator unit. The stator implements a load sensor and a load-dependent binding regulator; the binding is enhanced at high motor load for generating large torque and suppressed at low load for probably reducing futile energy consumption.

Cooperativity is central to the biological regulation[27]. A simple mechanism provided by the mutual dependence of the ligand-binding sites exhibits a steep nonlinear response, enabling robust and highly-sensitive regulation and signaling[28]. It would be natural to suppose that the BFM's torque regulation is highly optimized. However, conventional modeling ignores the cooperativity among stators for simplicity. Instead, a random packing of the stators without the stator-stator interaction is postulated[18,21,29].

In this work, we evaluate the stator-stator cooperativity to characterize the torque regulation by the BFM. We will show that the rotor-stator interaction is actually not favorable, and the stator-stator interaction is the driving force of the stator assembly (Fig. 1C). This makes a significant difference in the torque regulation by providing sophisticated torque regulation based on the discontinuous binary response of the torque to the load accompanied by hysteresis.

We exploit the dynamic load control by the electrorotation to study the stator remodeling process[20,21]. The stator assembly dynamics have been studied by controlling the expression level of the stators. By inducing the stator expression of the stator-less bacteria, a "resurrection" process characterized by the stepwise increase in the rotation rate was observed. The stator expression is the rate limiting for this resurrection approach, and a single trace takes more than 30 minutes typically. However, the dynamic and reversible load control[18,20–22] based on magnetic tweezers or electrorotation

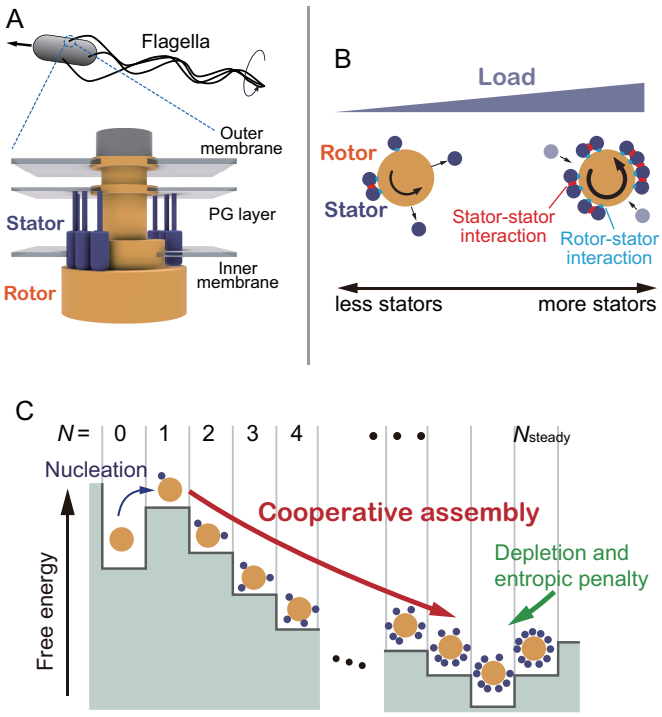

Figure 1. **A**, The BFM is a supramolecular complex with a diameter of about 45 nm spanning the membrane[2–5]. The motor consists of a rotor (yellow) and multiple torque-generating stators (blue). The stators have ion channels and generate torque at the interface with the rotor by exploiting the free energy change liberated by the ion currents through the channels. The stators interact with the rotor at its bottom part and are anchored to the rigid peptidoglycan (PG) layer with its top part[23–26]. **B**, The stators bind to and unbind from the motor. The stator binding to the motor is controlled by several factors, such as the load on the rotor and ion flux through the stator. **C**, We demonstrate that the stator-assembly dynamics are driven by the stator-stator interaction.

enable us to iterate many stator-assembly processes for statistical evaluation of the dynamics. We release all the bound stators by reducing the load on the motor and investigate the remodeling of the stators.

Results

Stator remodeling. Each experimental cycle consists of three phases: initial, assisting, and remodeling (Fig. 2A). In the initial phase, we observed a steady rotation for 10 s in the absence of an external load. The number of the bound stators, N, was estimated to be around 10 in this phase by the step analysis in the below. This relatively large value of N is due to the high viscous load on the tethered cell and is consistent with the previous results[20].

In the assisting phase, we assisted the rotation strongly for 10 s by the electrorotation for reducing the load on the motor. The rotation speed was accelerated to 300 - 600 Hz depending on the body dimension and the dielectric property of the cell.

In the remodeling phase, the assisting torque was turned off. The rotation rate vanished in the most traces (about 80% of the observed traces). The motor stalling indicates that all the bound stators are released under the low-load condition (see the inset of Fig. 2A). Some motors continued rotating while their rotation rate decreased much compared to the initial phase. This may be due to the insufficient magnitude and duration of the assisting torque[20,21].

The motor torque recovered to the initial steady level with successive discontinuous jumps, indicating the stepwise stator binding. The step size was similar independent of the torque magnitude. This is the characteristic of high load conditions such as the tethered cells[8]. The typical duration of each cycle was 120 s. However, we extended the remodeling phase when the recovery to the steady torque level was not sufficient. We repeated the cycles up to 15 times on the same motor.

Dwell time. In Fig. 2C, consecutive torque traces of a single motor are superposed. We found strong stochasticity, especially in the low torque region. The duration of the zero-torque state was typically long compared to the duration of the other states. That is, the binding of the first stator triggers the binding of more stators.

For the quantitative evaluation of the dynamics, we performed the step analysis of the traces based on the hidden-Markov modeling (red curve in Fig. 2B, see Methods)[30]. Note that, since we estimated N based on the motor torque, N is defined as the number of the bound stators that generate torque.

The distributions of the dwell time τ at N, $D_N(\tau)$, are shown in Fig. 3A (see Fig. S4 for individual distributions and the fitting by exponential functions). $D_0(\tau)$ has a long tail as implied in the trace (Fig. 2) and was significantly different from $D_N(\tau)$ for $N \geq 1$. Accordingly, the average, $\langle\tau\rangle_0$, was significantly larger than $\langle\tau\rangle_N$ for $N \geq 1$ (Fig. 3B). The distinct difference between the binding of the first stator and the binding of the second stator implies the existence of the stator-stator interaction.

Transition rates. Let $P_N(t)$ be the probability that the number of bound stators is N at time t. The Master equation for the

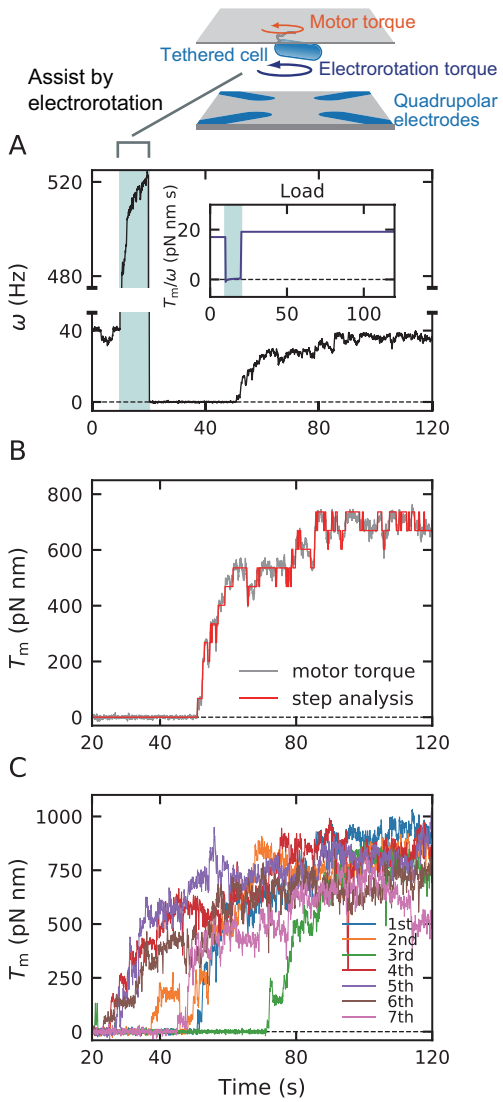

Figure 2. Rotation traces. **A**, A typical rotation trace. After initial 10-s phase, a strong assisting torque was applied for 10 s for releasing the stators from the motor by the electrorotation method[20]. The inset is the effective load on the motor T_m/ω. **B**, The motor torque (gray) was evaluated as described in[20] (see Methods for details). The stator number $N(t)$ (red) was estimated by a method based on the hidden-Markov modeling[30] (See Methods for details). **C**, Seven consecutive traces of a single motor are superposed.

dynamics of P_N is

$$\dot{P}_N = r^+_{N-1}P_{N-1} + r^-_{N+1}P_{N+1} - (r^+_N + r^-_N)P_N. \quad (1)$$

Here, $r^\pm_N$ are the on and off transition rates and satisfy $r^+_N + r^-_N = 1/\langle\tau\rangle_N$. While $\langle\tau\rangle_N$ expresses only the dwell duration, $r^\pm_N$ expresses the bias of the binding and unbinding events and contains fruitful information about the dynamics.

We obtained $r^\pm_N = n^\pm_N/[(n^+_N + n^-_N)\langle\tau\rangle_N]$ by counting the number of on and off transitions $n^\pm_N$ at each N (Fig. 3C) We found that r^+_N has a steep peak at $N = 2$, and r^-_N has a flat dependence on N at small N. This contradicts the conventional random-packing model that ignores the stator-stator interaction. The random-packing model postulates a linear dependence, $r^+_N \propto N_{\max} - N$ and $r^-_N \propto N$, where $N_{\max}$ is the maximum number of the stators that can bind to the motor, and $N_{\max} - N$ is the number of the unbound sites in the motor.

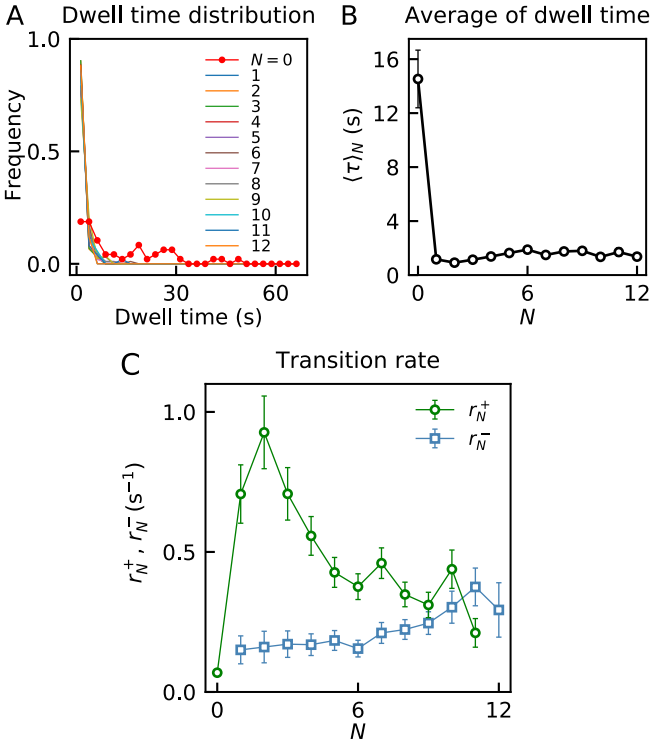

Figure 3. The transition rates and free-energy profile. **A**, Dwell time distribution for different stator number N. The bin width is 2.5 s. **B**, Average dwell time, $\langle\tau\rangle_N$, of the N state. The error bars indicate the standard error. **C**, The transition rates between different stator numbers, r_N^+ (green, circle) and r_N^- (blue, square). r_N^+ (r_N^-) is the transition rate from N to $N+1$ ($N+1$ to N). Note that these transition rates are different from the binding/unbinding rates of a single stator. The error bars correspond to the parameter estimation error of the Bayesian estimation. See Fig. S2 for all the traces used for the analysis.

The observation, $r_0^+ < r_1^-$ and $r_1^+ > r_2^-$, suggests that the binding of the first stator is not favorable, while the binding of additional stators are favorable. This suggests that the stator-stator binding affects both the binding and unbinding of the stators.

Free energy profile. Let G_N be the free energy profile of the stator assembly. The free energy difference, $\Delta G_N \equiv G_{N+1} - G_N$, was recovered using the detailed balance condition,

$$\Delta G_N = k_\mathrm{B} T \ln \frac{r_{N+1}^-}{r_N^+}, \tag{2}$$

where k_B is the Boltzmann constant, and T is the absolute temperature. Figure 4A shows that the binding of the first stator is unstable ($\Delta G_0 > 0$), while the succeeding bindings are stable ($\Delta G_N < 0$ for $1 \le N \le 10$). Since the stator-stator interaction does not affect the binding and unbinding of the first stator, ΔG_0 contains only the rotor-stator interaction. On the other hand, ΔG_N ($N \ge 1$) contains both the rotor-stator and stator-stator interactions. The above results indicate that the rotor-stator interaction is itself unstable, but is stabilized by the stator-stator interaction, that is, the cooperativity. ΔG_N increased with N and crossed zero in the vicinity of $N = 9$. Accordingly, G_N has a kinetic barrier at $N = 1$ and a minimum at $N \simeq 10$ (Fig. 4B), demonstrating the stator-assembly path.

Discussion

Cooperativity drives the stator assembly. We evaluated the kinetics (Fig. 3) and energetics (Fig. 4) of the stator assembly of the BFM by exploiting the dynamic load-control of the electrorotation method. The results clearly show that the binding of a single stator is not thermodynamically favorable, but the cooperativity provided by the stator-stator interaction stabilizes the stator binding to the rotor (Fig. 1C). Thus, we conclude that the cooperativity of the stators drives the stator assembly. Our analysis is mainly based on the step analysis of the torque traces. Despite that the traces were noisy, we exploited the hidden Markov modeling for robust step finding. See Section S1 of Supplementary Information for the validation of the method.

In the following, the above conclusion will be further validated by reproducing the free energy profile based on a simple and intuitive model. First, we will evaluate the effect of the cooperativity, that is, the stator-stator interaction. Second, the model will be modified to incorporate the depletion effect.

Model of the stator assembly. Let E be the energy of a microscopic state,

$$E = n\varepsilon + m\sigma. \tag{3}$$

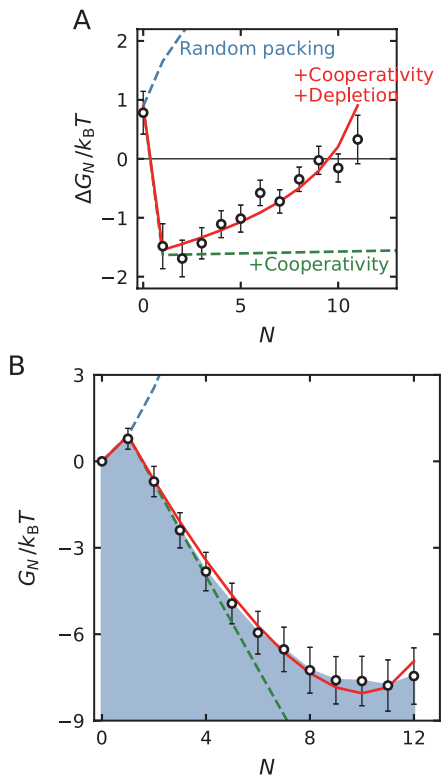

Figure 4. Free energy profile. **A**, The free energy difference, $\Delta G_N = G_{N+1} - G_N$, obtained by (2). The model calculation (lines) and experimental data (circle) are superposed. The model calculation is based on (4) and (5) for the 2^{N_max} configurations by a random packing model (blue), a model with stator-stator interaction (green), and a model with the stator-stator interaction and the depletion effect (red). We used $N_\mathrm{max} = 15$, $\varepsilon = 3.6 k_\mathrm{B}T$, $\sigma = -5.2 k_\mathrm{B}T$, and $N_0 = 12$. See Fig. S5 for the details of the fitting. **B**, The free energy profile, G_N. The error bars correspond to the parameter estimation error of the Bayesian estimation.

Here, a microscopic state refers to a single configuration of the bound stators and is defined by $\{s_1, s_2, \ldots, s_{N_{\max}}\}$. $s_k \in \{0,1\}$ indicates the occupancy of the k-th site and has a periodic boundary, $s_{N_{\max}+1} = s_1$. $n = \sum_k s_k$ and $m = \sum_k s_k s_{k+1}$ are the numbers of the bound stators and the number of the stator-stator interface, respectively, contained in the configuration. ε and $\sigma(<0)$ are the rotor-stator interaction energy and the stabilization energy by the stator-stator interaction, respectively. See Section S2 of Supplementary Information for the mapping of the present model into the Ising model.

Note that ε contains not only the rotor-stator interaction but also the chemical potential of the diffusing stator in the membrane and the stabilization effect by the rotation. The stabilization by the rotation was proposed to explain the load dependence of the stator assembly[18]. The magnitude of the stabilization is determined by the load on each stator[21]. However, as noted, since the load on each stator does not change with N for the tethered cell with the high load[8], ε is assumed to be independent of N.

The free energy profile is given by

$$G_N = -k_{\mathrm{B}}T \ln \sum_{i\,(n(i)=N)} e^{-\frac{E(i)}{k_{\mathrm{B}}T}} = N\varepsilon + G_N^{\mathrm{ss}}, \tag{4}$$

$$G_N^{\mathrm{ss}} = -k_{\mathrm{B}}T \ln \sum_{i\,(n(i)=N)} e^{-\frac{m(i)\sigma}{k_{\mathrm{B}}T}}. \tag{5}$$

Here, i is the label for a microscopic state. G_N^{ss} implements both the stator-stator interaction energy σ and the configuration entropy. The summation is calculated only for the states with $n(i) = N$. The free energy change associated with a single stator binding is

$$\Delta G_N = \varepsilon + \Delta G_N^{\mathrm{ss}}, \qquad \Delta G_N^{\mathrm{ss}} = G_{N+1}^{\mathrm{ss}} - G_N^{\mathrm{ss}}. \tag{6}$$

We assume that the stators bind to specific discrete binding sites like the Langmuir adsorption model[31] for simplicity. However, from the structural point of view[5], it would be more likely that the binding takes place continuously at the rotor periphery like the random sequential adsorption model[32]. It was shown that this difference is not effective for the random packing model[18]. Even if the effect is not negligible, the effect is expected to be limited for large N, where the binding history determines the volume of the remaining space for the stator binding.

Stator-stator interaction. The random-packing model ($\sigma = 0$) has been used conventionally[18,21,29]. This model neglects the effect of the stator-stator interaction on the stator assembly. Then, the free energy is given by the configuration entropy, $G_N^{\mathrm{ss}} = -k_{\mathrm{B}}T \ln[N_{\max}!/N!(N_{\max}-N)!]$, since the bound stators distribute uniformly at the rotor periphery without forming localized clusters. $\Delta G_N = \varepsilon + k_{\mathrm{B}}T \ln \frac{N+1}{N_{\max}-N}$ increases continuously with N and does not reproduce the large gap between ΔG_0 and ΔG_1 (Fig. 4A, blue curve).

On the other hand, the gap was reproduced by incorporating the stator-stator interaction ($\sigma < 0$) (Fig. 4A, green curve). The gap appears because the stator-stator interaction affects only G_N for $N \geq 2$. This validates that the stator-stator interaction plays an essential role in the stator assembly. We obtained $\varepsilon = 3.6 k_{\mathrm{B}}T$ and $\sigma = -5.2 k_{\mathrm{B}}T$ by fitting the experimental curve at small N by (6). Note that ΔG_N at small N are approximately given by $\Delta G_0 = \varepsilon - k_{\mathrm{B}}T \ln N_{\max}$ and $\Delta G_1 \simeq \varepsilon + \sigma$ unless $|\sigma|$ is very small (see SI text for details). While the values of ε and σ vary slightly with the analysis parameters (Fig. S1), the qualitative curve shapes were robust. It would be intriguing to evaluate ε and σ by different approaches, including structural studies.

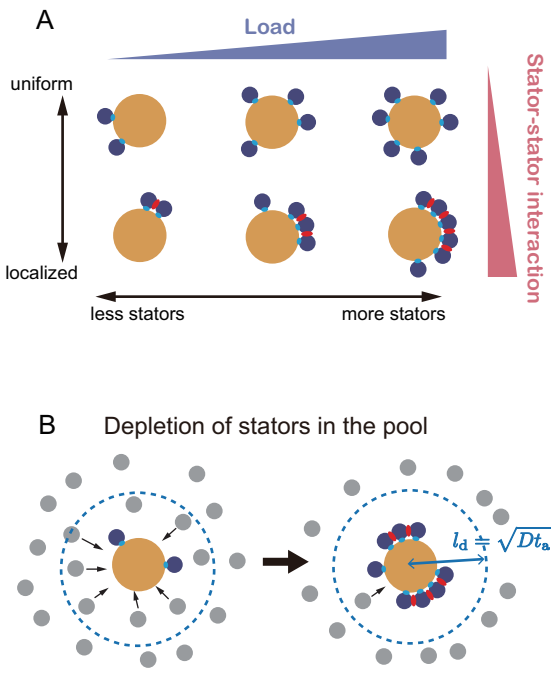

Figure 5. **A**, Stator-stator interaction localizes the bound stators. **B**, Depletion of stators. Since the number of the stators accessible by the motor (the stators inside the blue dashed circle) is finite, the binding rate is suppressed as the stators bind to the motor. D is the diffusion coefficient of the stator in the membrane. t_{a} is the typical time scale for the stator assembly. l_{d} is the diffusion length during t_{a}.

In the presence of stator-stator interaction, the stators do no longer distribute randomly at the rotor periphery but may form localized clusters (Fig. 5A). The larger $|\sigma|$ is, the more likely the stators localize. Then, the stators tend to bind to and unbind from only the cluster edge, and ΔG_N becomes less independent of N, exhibiting a flat profile (Fig. 4A, green curve). However, this behavior deviates from the experimental curve at a large N.

Depletion effect. For better modeling at large N, we will incorporate the depletion effect (Fig. 5B). The stators alternate between the motor and the membrane pool close to the motor[9]. Let N_0 be the effective number of the stators accessible by the motor. A simple and intuitive postulate would be that the binding rate is proportional to the number of the freely-diffusing stators, $N_0 - N$, which decreases with the stator binding. This depletion effect increases ΔG because the stator binding at large N is suppressed unless $N_0 \gg N_{\max}$ (Fig. 4B). Note that the depletion of the remaining space in the motor due to bindings is already included in (5).

The free energy change associated with the depletion is given by $\Delta G_N^{\mathrm{dep}} = -k_{\mathrm{B}}T \ln \frac{N_0 - N}{N_0}$ and increases with N monotonically. Here, the normalization factor, which can be chosen arbitrary, is chosen as $1/N_0$ for simplicity. We regard that the

stator-membrane interaction energy is already included in ε. Now, (6) is modified to

$$\Delta G_N = \varepsilon + \Delta G_N^{\mathrm{ss}} + \Delta G_N^{\mathrm{dep}}. \tag{7}$$

We found that the experimental curve was well fitted by (7) with the fitting parameter $N_0 = 12$ (Figs. 4A and B, red curve). The independent estimation of N_0 based on the diffusion dynamics of the stators in the membrane pool yields a similar value (see Section S3 of Supplementary Information). This supports the validity of our model.

Kinetics. We found a characteristic dependence of $r_N^{\pm}$ on N (Fig. 3C). r_N^{+} has a steep peak at $N = 2$. The increase in r_N^{+} at a small N indicates that the binding is affected by the stator-stator interaction. The stator binding is thought to be comprised of two steps. The first step is the collision of the stator to the rotor accompanied by an imperfect binding. The second step involves the rigid fixation on the PG layer, which enables the torque generation. The stator-stator interaction may stabilize the imperfectly-bound stators and enhance the fixation on the PG layer (Fig. 1A). Then, r_N^{+} increases with N because it is more probable for the bound stators to interact with other stators at a larger N. At large N, r_N^{+} decreases due to the depletion of the remaining space ($N_{\max} - N$) as well as the depletion of the stators in the membrane pool ($N_0 - N$). The peak is explained by the combination of these two counteracting effects.

We obtained similar values of r_N^{-} for small N, which is a characteristic of the stator clustering. As noted, in the random packing model, r_N^{-} is proportional to N. The increase in r_N^{-} with N for large N is reasonable since r_N^{-} is the rate that one of the N bound stators dissociates.

It was recently reported that the dwell time distribution $D_N(\tau)$ contains two time scales for, at least, $N = 4$, 5, and 6[29]. We could not resolve the time scales in $D_N(\tau)$ for $N > 0$ (Fig. S4). This discrepancy might be caused by the difference in the viscous load on the motor. The previous work used a micrometer-sized particle as the rotation probe, which has a lower viscous load than the tethered cell and can detect a faster event. However, $D_0(\tau)$ seems to have multiple time scales (Fig. S4). The slow dynamics of $N = 0$ state might have made the time-scale difference apparent.

Discontinuous transition. The stator-stator interaction alters the torque regulation manner qualitatively (Fig. 6). The analysis by random-packing model suggested that the rotor-stator interaction energy, ε, decreases linearly with the load per stator[21]. Whereas it is not determined how the stator-stator interaction affects this dependence, it is still expected that ε indicates the magnitude of the load per stator (Fig. 6A and C).

As illustrated in Fig. 6, the significant difference in the presence and absence of the stator-stator interaction is that the former shows discontinuous transition while the latter shows the continuous transition. The discontinuous transition acts as a binary switch between zero torque and large torque in response to the load. Such a steep change in the motor torque enables a highly-sensitive response to the load. As well, the prominent characteristic of the discontinuous transition is that

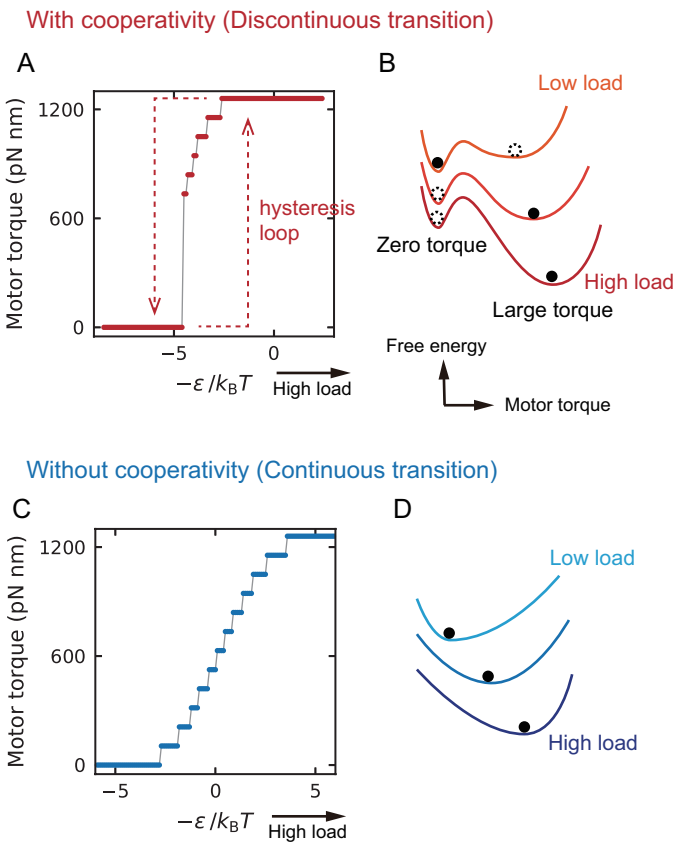

Figure 6. Autonomous torque regulation by the motor in response to the load change. The motor torque is calculated by multiplying the mean torque per stator, 105 pN nm (Fig. S3), and the minimum of G_N calculated numerically in the presence (**A**) or in the absence (**C**) of stator-stator interaction. The depletion effect is implemented in both **A** and **C**. Torque exhibits a first-order discontinuous transition with the stator-stator interaction, while a second-order continuous transition is expected without the stator-stator interaction. The symbols correspond to the equilibrium values of the motor torque. The actual dynamics proceed like the dashed arrows. The dashed arrows in **A** are the hypothetical hysteresis curves. **B**, **D**, Schematic of the free energy profile. Closed circles and dashed open circles denote the stable states and the metastable states, respectively. See Fig. S6 for the details.

it possesses a meta-stable state and, therefore, exhibits a hysteresis behavior (Fig. 6A, B). The hysteresis provides robust response to the noise. Without the hysteresis, the motor torque fluctuates largely by the noise passing over the transition point. The binary behavior and the robustness to the noise are also favorable to ensure that the rotor does not rotate during the flagellar-motor assembly. Note that the discontinuous transition is consistent with the previous observation that there is a threshold load below which the stators dissociate[21].

Acknowledgements. We thank Yoshiyuki Sowa, Yohei Nakayama, and Kazuo Sasaki for helpful discussions. This work was supported by JSPS KAKENHI (16H00791 and 18H05427).

Methods

The experimental system is basically the same as the system described in the previous work[20].

Cell preparation. *Salmonella* strain YSC2123, which lacks *motA*, *motB*, *cheY*, *fimA*, and *fliC* (204–292), was transformed with a plasmid encoding wild-type *motA/motB*[33] (referred to as a wild-type). Cells were grown in L-broth containing 100 μg/ml ampicillin and 0.2% arabinose (for the expression of the MotA and MotB) for overnight at 30 °C with shaking. L-broth was prepared as described previously[34]. The buffer was replaced with the observation buffer (10 mM MOPS(3-Morpholinopropanesulfonic acid) and 10 mM KCl adjusted to pH8.3 with KOH).

Microscopy. We observed the rotation of a tethered cell at room temperature (24°C) on a phase-contrast upright microscope (Olympus BX51WI, Japan) with a 60× objective lens (Olympus, NA=1.42), at 4,000 Hz using a high-speed CMOS camera (Basler, Germany), high-intensity LED (623 nm, 4.8W, Thorlabs, NJ) for illumination, and a laboratory-made capturing software developed on LabVIEW (National Instruments, TX). The angular position of the cellular body was analyzed by an algorithm based on a principal component analysis of the cell image. We used 50 mg/ml Perfect Block (MobiTec, Germany) as the blocking agent to suppress the interaction between the cell body and the glass surface. The chamber height was about 12 μm.

Electrorotation. A 10-MHz sinusoidal voltage with a phase shift of $\pi/2$ was induced on the four electrodes patterned on the bottom glass surface (Fig. 1A). The distance between the electrodes is 47 μm. The signal was generated by a function generator (nf, Japan) controlled by PC and divided by 180° phase distributors (Thamway, Japan). They were amplified by four amplifiers (Analog Devices, MA) and loaded on the electrodes. This generates an electric field rotating at 10 MHz in the center of the electrodes and induces a dipole moment rotating at 10 MHz on the cell body. Since there is a phase delay between the electric field and the dipole moment, the cell body is subjected to a constant torque. The torque magnitude is proportional to the square of the voltages' amplitude V_0. We modulated V_0 by a signal generated by the multifunction board (National Instruments) equipped on PC. The camera and amplitude signal were synchronized at a time difference of less than one microsecond. We applied an external torque with a time-dependent magnitude, as indicated in the main text, with superposed by a 1000-Hz small sinusoidal torque for the torque calibration. See the references[20,35] for the details of the torque calibration.

Torque evaluation and step analysis. We observed more than 300 traces of the stator remodeling process. However, the step analysis was possible for only 38 traces (10 cells) due to the noise.

We divided the trajectory into windows with a length of 512 frames with 128-frame shifts and calculated γ, ω, and T_m in each window. The frictional coefficient, γ, was calculated based on the velocity fluctuation and the fluctuation-dissipation theorem[20]. The torque trajectory was further smoothed by a moving average with a window size of 20 points.

We performed step analysis of the torque traces using an algorithm based on the hidden Markov model (HMM)[30,36]. We used the Gaussian HMM module included in the hmmlearn library of Python. The torque per stator, which was assumed to be the same for all N, was estimated based on the torque distribution. The HMM estimates the variance of the emission probability, the transition probabilities of each state, and $N(t)$ with the maximum likelihood. See Fig. S3 for the distribution of the torque per stator. The average was 105 ± 20 pN nm (mean ± SD), which is consistent with the previous results[20].

References

1. Horstmann, J. A. *et al.* Flagellin phase-dependent swimming on epithelial cell surfaces contributes to productive salmonella gut colonisation. *Cell. Microbiol.* **19**, e12739 (2017).
2. Berg, H. C. The rotary motor of bacterial flagella. *Annu. Rev Biochem.* **72**, 19–54 (2003).
3. Berry, R. M. & Armitage, J. P. The bacterial flagella motor. *Adv Microb Physiol.* **41**, 291–337 (1999).
4. Sowa, Y. & Berry, R. M. Bacterial flagellar motor. *Q. Rev. Biophys.* **41**, 103–132 (2008).
5. Nakamura, S. & Minamino, T. Flagella-driven motility of bacteria. *Biomolecules* **9**, 279 (2019).
6. Magariyama, Y. *et al.* Very fast flagellar rotation. *Nature* **371**, 752–752 (1994).
7. Block, S. M. & Berg, H. C. Successive incorporation of force-generating units in the bacterial rotary motor. *Nature* **309**, 470–2 (1984).
8. Ryu, W. S., Berry, R. M. & Berg, H. C. Torque-generating units of the flagellar motor of escherichia coli have a high duty ratio. *Nature* **403**, 444 (2000).
9. Leake, M. C. *et al.* Stoichiometry and turnover in single, functioning membrane protein complexes. *Nature* **443**, 355 (2006).
10. Yuan, J. & Berg, H. C. Resurrection of the flagellar rotary motor near zero load. *PNAS* **105**, 1182 (2008).
11. Fukuoka, H., Wada, T., Kojima, S., Ishijima, A. & Homma, M. Sodium-dependent dynamic assembly of membrane complexes in sodium-driven flagellar motors. *Mol. Microbiol.* **71**, 825–835 (2009).
12. Tipping, M. J., Delalez, N. J., Lim, R., Berry, R. M. & Armitage, J. P. Load-dependent assembly of the bacterial flagellar motor. *mBio* **4**, 00551–13 (2013).
13. Tipping, M. J., Steel, B. C., Delalez, N. J., Berry, R. M. & Armitage, J. P. Quantification of flagellar motor stator dynamics through in vivo proton-motive force control. *Mol. Microbiol.* **87**, 338–347 (2013).
14. Lo, C.-J., Sowa, Y., Pilizota, T. & Berry, R. M. Mechanism and kinetics of a sodium-driven bacterial flagellar motor. *PNAS* **110**, E2544–E2551 (2013).
15. Lele, P. P., Hosu, B. G. & Berg, H. C. Dynamics of mechanosensing in the bacterial flagellar motor. *PNAS* **110**, 11839–44 (2013).
16. Nord, A. L., Sowa, Y., Steel, B. C., Lo, C.-J. & Berry, R. M. Speed of the bacterial flagellar motor near zero load depends on the number of stator units. *PNAS* **114**, 11603–11608 (2017).
17. Wang, B., Zhang, R., & Yuan, J. Limiting (zero-load) speed of the rotary motor of escherichia coli is independent of the number of torque-generating units. *PNAS* **114**, 12478–12482 (2017).
18. Nord, A. L. *et al.* Catch bond drives stator mechanosensitivity in the bacterial flagellar motor. *PNAS* **114**, 12952–12957 (2017).
19. Baker, A. E. & O'Toole, G. A. Bacteria, rev your engines: Stator dynamics regulate flagellar motility. *J. Bact.* **199**, e00088–17 (2017).
20. Sato, K., Nakamura, S., Kudo, S. & Toyabe, S. Evaluation of the duty ratio of the bacterial flagellar motor by dynamic load control. *Biophys. J.* **116**, 1952–1959 (2019).
21. Wadhwa, N., Phillips, R. & Berg, H. C. Torque-dependent remodeling of the bacterial flagellar motor. *PNAS* 201904577 (2019).

22. Nirody, J. A., Nord, A. L. & Berry, R. M. Load-dependent adaptation near zero load in the bacterial flagellar motor. *J. Roy. Soc. Int.* **16**, 20190300 (2019).

23. Kojima, S. *et al.* Stator assembly and activation mechanism of the flagellar motor by the periplasmic region of MotB. *Mol. Microbiol.* **73**, 710–718 (2009).

24. Zhu, S. *et al.* Conformational change in the periplamic region of the flagellar stator coupled with the assembly around the rotor. *PNAS* **111**, 13523–13528 (2014).

25. Terahara, N. *et al.* Na^+-induced structural transition of MotPS for stator assembly of the Bacillus flagellar motor. *Sci. Adv.* **3**, eaao4119 (2017).

26. Kojima, S. *et al.* The helix rearrangement in the periplasmic domain of the flagellar stator b subunit activates peptidoglycan binding and ion influx. *Structure* **26**, 590–598.e5 (2018).

27. Williamson, J. R. Cooperativity in macromolecular assembly. *Nat. Chem. Biol.* **4**, 458–465 (2008).

28. Pauling, L. The oxygen equilibrium of hemoglobin and its structural interpretation. *PNAS* **21**, 186–191.

29. Shi, H., Ma, S., Zhang, R. & Yuan, J. A hidden state in the turnover of a functioning membrane protein complex. *Sci. Adv.* **5**, eaau6885 (2019).

30. Bishop, C. M. *Pattern Recognition and Machine Learning* (Springer, 2006).

31. Langmuir, I. The adsorption of gases on plane surfaces of glass, mica and platinum. *J. Am. Chem. Soc.* **40**, 1361–1403 (1918).

32. Evans, J. W. Random and cooperative sequential adsorption. *Rev. Mod. Phys.* **65**, 1281–1329 (1993).

33. Morimoto, Y. V., Che, Y. S., Minamino, T. & Namba, K. Proton-conductivity asssay of plugged and unplugged MotA/B proton channel by cytoplasminc pHluorin expressed in Salmonella. *FEBS Lett.* **584**, 1268–72 (2010).

34. Minamino, T., Imae, Y., Oosawa, F., Kobayashi, Y. & Oosawa, K. Effect of intracellular pH on rotational speed of bacterial flagellar motors. *J. Bacteriol.* **185**, 1190–1194 (2003).

35. Toyabe, S., Watanabe-Nakayama, T., Okamoto, T., Kudo, S. & Muneyuki, E. Thermodynamic efficiency and mechanochemical coupling of F_1-ATPase. *PNAS* **108**, 17951–17956 (2011).

36. Toyabe, S., Ueno, H. & Muneyuki, E. Recovery of state-specific potential of molecular motor from single-molecule trajectory. *EPL* **97**, 40004 (2012).